In-Situ Observation Combined with Numerical Simulation of the Solidification and Subsequent Cooling Process for Hot Stamping Steel

Jingzhou Lu[1,2] · Jiaxi Chen[1] · Weiming Pan[1] · Wanlin Wang[1] · Kun Dou[1,2]

Abstract

In this study, the solidification and subsequent cooling processes of hot stamping steel during thin slab casting have been investigated using high-temperature confocal in-situ observation experiments and finite element numerical simulations based on the calculation results of phase evolution diagrams. The numerical simulation results reveal that different regions of the cast slab exhibited varying solidification times/cooling rates, with the longest solidification time occurring at the center of the slab, approximately 77.5 s, and the shortest at the corners, around 2.1 s. Considering these findings, in-situ observation experiments have been conducted under cooling rates of 10, 50, 150, and 1000 °C/min, revealing that both solidification and solid-state transformation events are delayed with increasing cooling rates. Notably, under higher cooling rates, the peritectic reaction process exhibit blocky transformation. Based on the findings, this study establishes relationships between the ferrite growth rate/secondary dendrite arm spacing and cooling rate for hot stamping steel. Additionally, potential optimization strategies for continuous casting and secondary cooling process parameters are suggested to enhance the sophistication of thin slab production processes. These optimization methodologies are informed by guiding experiments conducted in conjunction with numerical simulations, ultimately facilitating the optimization of practical production practices.

Keywords In-situ observation · Numerical simulation · Hot stamping steel · Cooling rate · Solidification structure

1 Introduction

With the development of the society and economy, the global steel market competition is becoming increasingly intense. Short-process casting techniques, such as thin slab casting and thin strip casting, hold tremendous potential in providing more efficient, economical, and environmentally friendly methods for steel production [1]. Additionally, with the increasing demands for lightweight and crash safety in automobiles, the steel industry is continuously evolving toward high-strength and high-ductility automotive steels, among which hot stamping steel is widely used [2]. Hot stamping is the key forming technology to manufacture automobile components with high strength and hot stamping steel and its manufacturing technology experienced a fast development in the past decade [3].

The solidification of molten steel is a complex process involving various phenomena such as crystal growth, phase transitions, and defect formation. High-temperature confocal microscopy offers in-situ observations, enabling researchers to gain an in-depth understanding of the dynamic evolution of this process [4, 5]. This includes the growth and orientation of crystals, phase transitions, and the formation of defects. Wang et al. investigated the peritectic solidification process of Fe–Mn–Al–C steel with 5.56 wt% Mn in-situ using HT-CLSM (high temperature confocal laser scanning microscopy), and the effects of the cooling rate on the kinetics of the peritectic transformation and the solidification microstructure have been investigated systematically [6]. Zargar et al. utilized synchrotron white beam X-ray for in-situ observation of the solidification process in hypo- and hyper-peritectic steel grades under a constant slow cooling rate of 5 K/min and investigated the effect of carbon content and specimen thickness on the δ to γ transformation mode [7]. Chen et al.

✉ Kun Dou
Kun.Dou@csu.edu.cn

1 School of Metallurgy and Environment, Central South University, Changsha 410083, Hunan, China

2 Xiangjiang Laboratory, Changsha 410205, Hunan, China

systemically investigated the microstructure evolutions of 300 M steel under various cooling rates (0.01–100 °C/s) and observed pearlite, bainite, and martensite to form at the cooling rate range of 0.01–0.15, 0.03–1, and 0.3–100 °C/s, respectively [8].

The numerical simulation method has been widely used in the production of steel continuous casting processes, providing some references and optimization directions for the smooth progress of production [9, 10]. Specifically, numerical simulation can offer the actual temperature distribution and solidification conditions of the ingot under specific processes, thereby serving as a basis for improving continuous casting production process parameters, including parameters in the secondary cooling zone. Yao et al. used a segmented numerical coupling model to investigate the heat transfer, solute transport, and solidification profile of liquid steel under three different nozzle configurations [11]. Sadat et al. simulated the three-dimensional turbulence and solidification process in the mold and secondary cooling zone of a thin slab continuous caster, and the model coupled and solved the k–ε flow and heat transfer equations simultaneously [12].

Numerical simulation assisted experiment exploration has become an efficient and comprehensive research method [13]. Nomoto et al. proposed a microstructure-based multiscale simulation framework using various commercial simulation software applications to simulate the microstructure evolution and elastoplastic deformation behavior of the materials [14].

Therefore, this study focuses on assisting experiments with numerical simulation processes. The non-equilibrium solidification phase diagrams of hot stamping steel under different cooling rates are first calculated using CAL-PHAD technology, providing realistic material properties as model input. On this basis, the heat transfer and solidification of the hot stamping steel production process in thin slab casting are simulated using a coupled macro finite element model, obtaining the temperature and solidification time at different locations of the cast slab. Finally, based on the aforementioned calculations, a HT-CLSM in-situ observation experiment is designed to explore the solidification process of hot stamping steel under different cooling rates. Based on the experiment and simulation results, functional relationships between ferrite growth rate/secondary dendrite arm spacing and cooling rate are obtained for hot stamping steel. Also, possible optimization methods for continuous casting and secondary cooling process parameters are proposed to advance the maturity of thin slab production processes. The optimization is achieved through guiding experiments with numerical simulations and ultimately serving the optimization of actual production.

2 Numerical Simulation and Experiment

Table 1 is the main chemical compositions of hot stamping steel.

2.1 Main Idea and Objectives

In Fig. 1, a comprehensive flow chart illustrating the full-process of in-situ observation combined with numerical simulation of the solidification and subsequent cooling process of hot stamping steel is presented. This flow chart encompasses three fundamental components: determination of thermophysical parameters and phase diagrams under non-equilibrium solidification, numerical simulation of the cooling process and in-situ observation of the cooling process. As the thin slab casting process is known for rapid cooling rate and significant variations in temperature distributions, the process parameters also need to be flexibly changed. Through numerical simulations, temperature field, fraction solid, and solidification time at different positions can be obtained, allowing for the calculation of solidification cooling rates at different positions. Based on simulation results, high temperature confocal microscopy experiments are conducted to observe solidification and solid-state phase transitions under different cooling rates, followed by an analysis of the possible problems caused by different cooling rates of thin slab casting process (the hot stamping steel). The corresponding improvement methods are ultimately proposed based on the simulation and experiment results.

2.2 Calculation of Solidification and Cooling Phase Diagram For Hot Stamping Steel

The solidus/liquidus temperature and equilibrium phase evolution diagram of hot stamping steel is calculated based on CompuThermal LLC databases [15] imbedded into ProCAST [16]. The liquidus temperature of the hot stamping steel is 1508 °C, while the solidus temperature is 1446 °C. From the calculation results (Fig. 2), as the temperature decreases, liquid phase first transforms into δ-Fe phase. At 1490 °C, formed δ-Fe phase and liquid phase together transform into γ-Fe phase. At 1470 °C, almost the entire liquid phase has transformed into γ-Fe phase. Subsequently, at 800 °C, austenite begins to transform into α-Fe phase, accompanied by the formation of cementite and carbides.

For non-equilibrium solidification and cooling process, the back diffusion micro-segregation model is applied to describe the solute transport and distribution among different

Table 1 Main chemical compositions of hot stamping steel (wt%)

C	Mn	Si	Cr	Fe
0.23	1.2	0.25	0.2	Bal.

Fig. 1 Flow chart of in-situ observation combined with numerical simulation of the solidification and subsequent cooling process of hot stamping steel
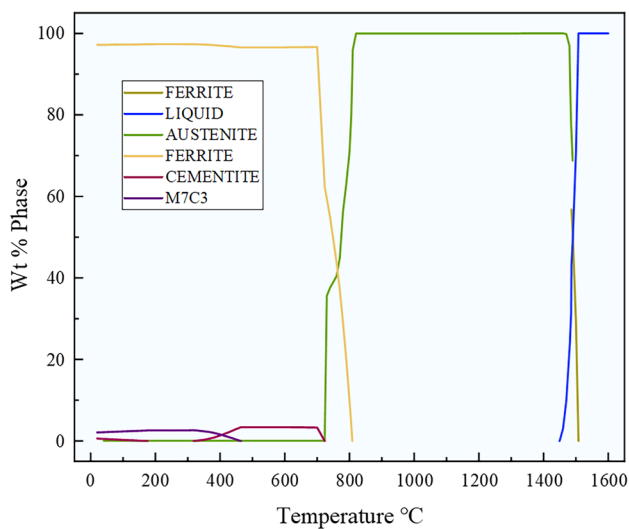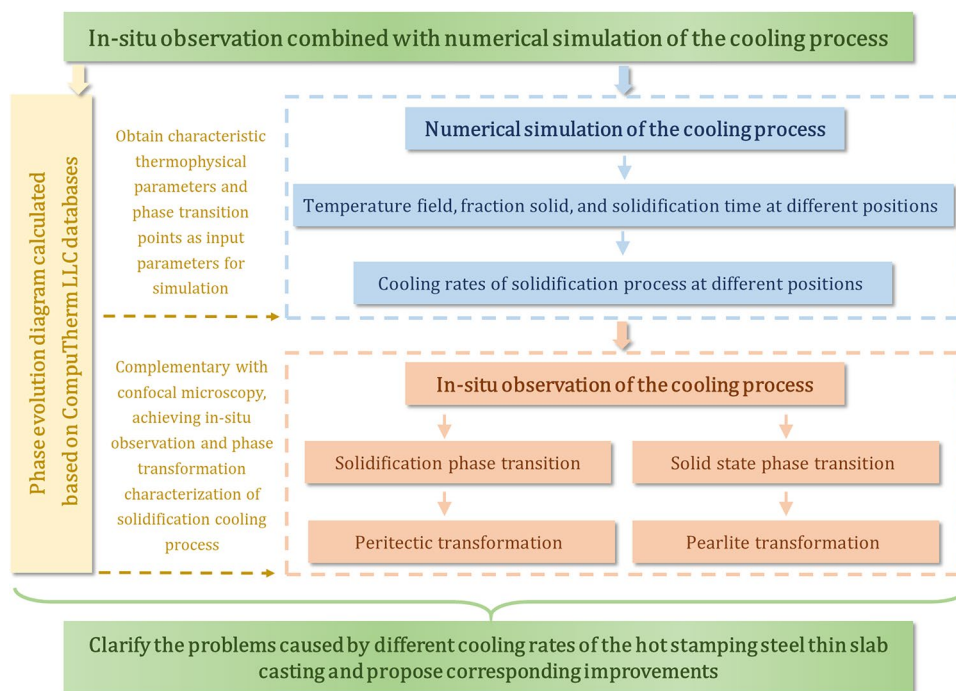

Fig. 2 The temperature and phase evolution diagram of hot stamping steel

phases [17–19]. Then the phase evolutions during solidification process of hot stamping steel at different cooling rates are calculated. In Fig. 3, the cooling rates are 1000, 150, 50 and 10 °C/min, under which the solidification process shows little variation in phase transformation, all undergoing the peritectic transition. The significant differences lie in the solid-state phase transitions. At the highest cooling rate (1000 °C/min), at 715 °C, there is transformation from γ-Fe phase to pearlite, resulting in a minimal amount of α-Fe phase with the maximum proportion of approximately 1.5%. Subsequently, a small amount of bainite forms at 555 °C, and at 395 °C, the γ-Fe phase begins to transform into martensite. Eventually, almost all phases transform into martensite. At the extremely high cooling rate, the most notable feature is the complete transformation into martensite. At the cooling rate of 150 °C/min, the onset temperature of the transformation from γ-Fe phase to pearlite has increased to 740 °C. The maximum proportion of α-Fe phase derived from γ-Fe phase transformation also reaches 8.0%. The subsequent transformation into bainite has increased, but at this point, the predominant phase is still martensite, derived from the transformation of γ-Fe phase, constituting approximately 80%. At the cooling rate of 50 °C/min, the temperature at which α-Fe phase appears increases to 750 °C, and the final proportion of α-Fe phase increases to 17%. At the cooling rate of 10 °C/min, the temperature at which α-Fe phase appears further increases to 765 °C, and the final proportion of α-Fe phase increases to 48%. Under this cooling rate, there is no formation of martensite.

According to the calculated results, as the cooling rate decreases, the temperature at which γ-Fe phase undergoes pearlite transformation increases, and the final proportion of α-Fe phase content increases.

2.3 Numerical Simulation of Thin Slab Casting Temperature Field

The ProCAST code is applied to calculate the temperature field at different positions (Fig. 4) during thin slab casting process [20–22]. The model utilizes a two-dimensional slice, representing a cross-section of the continuously advancing
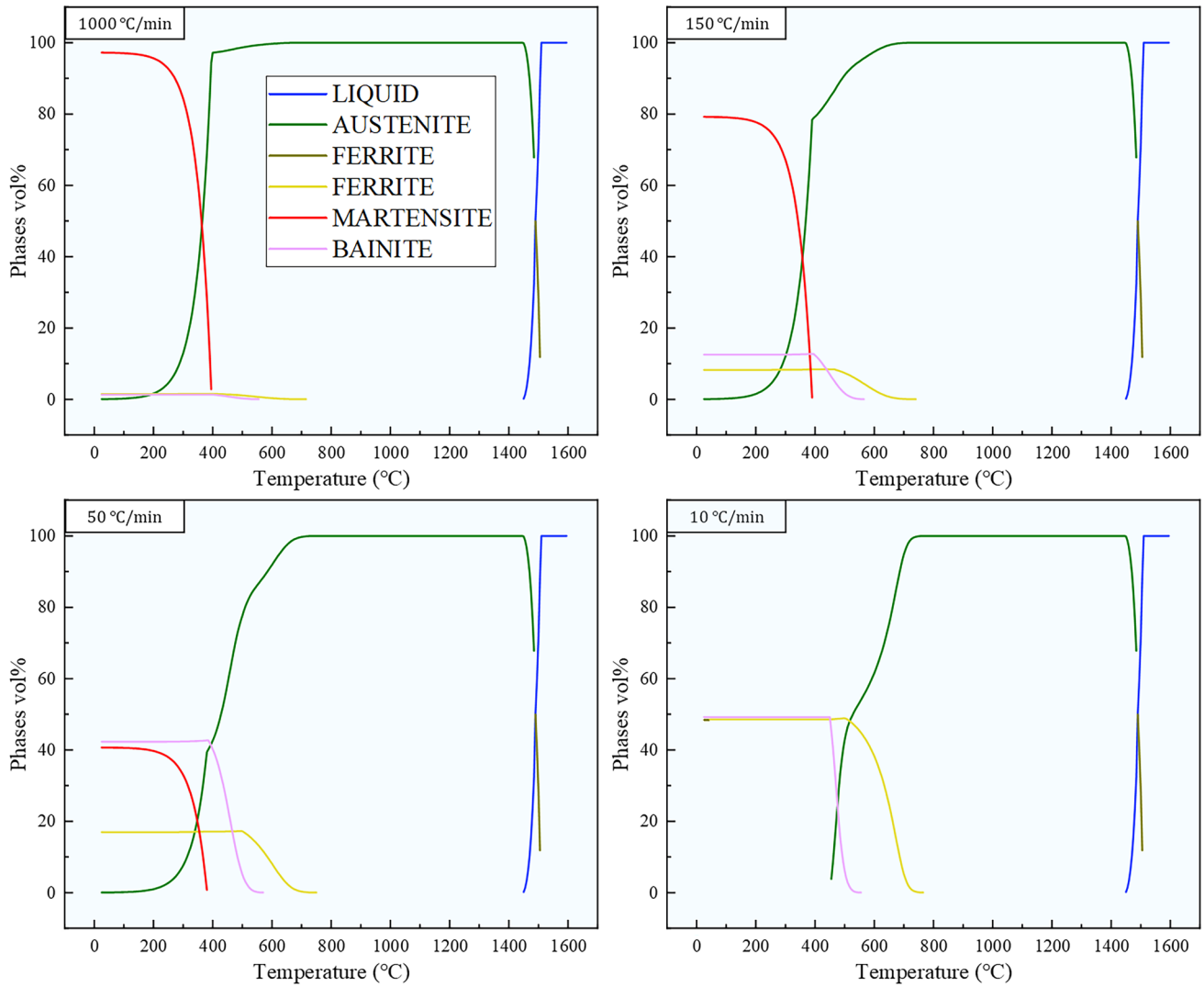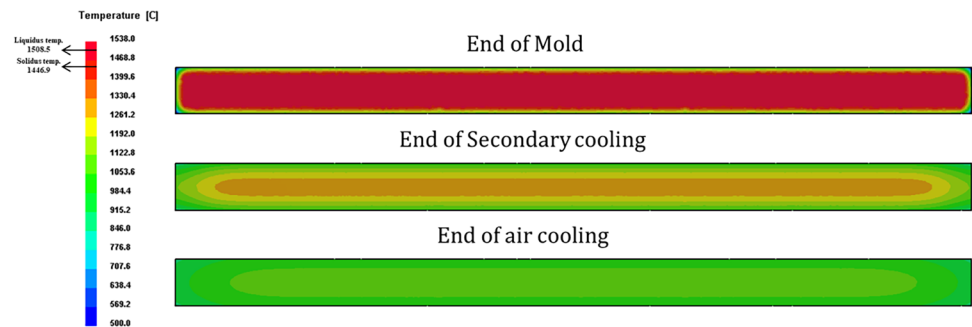
Fig. 3 Phase evolutions during solidification process of hot stamping steel at different cooling rates

Fig. 4 Numerical simulation results of temperature field at different positions

casting slab during the thin slab casting process. Different time points in the simulation calculations represent the actual conditions of the casting slab at different positions throughout the entire casting process. Actual temperature measurements are taken at the secondary cooling end of the thin slab casting production line. The temperatures measured at the center of the slab, the center of the slab wide surface, and the center of the slab narrow surface are 1150 °C, 996 °C, and 980 °C, respectively. Based on the numerical simulation model of this study, the corresponding

temperatures are calculated to be 1177 °C, 981 °C, and 997 °C, respectively. The error range is 1.5%–2.3%, which is relatively small, and this model can be considered as a high accuracy model. At the end of the mold, the central majority region of the thin slab is still at a high temperature, in a liquid state, with only the outermost layer of molten steel solidified, forming a solidified slab shell. By the end of the secondary cooling, the thin slab has fully solidified, but the center temperature remains slightly higher than that of the boundary. In other words, closer to the center, the cooling rate of the molten steel is slower, while the outer layer has a significantly faster cooling rate. Finally, at the end of the air cooling, the overall temperature of the thin slab tends to be uniform, approximately around 900 °C.

Simultaneously, the actual solidification situation can be inferred based on the fraction solid at different locations (Fig. 5). Within the first 0–20 s, the casting slab is inside the mold, and the solidification shell has initially formed, but there is still a significant liquid core in the central region. After 20 s, the casting slab enters the secondary cooling stage, and the solidification shell slowly grows inward. By 144 s, the casting slab has completely solidified.

Figure 6 illustrates the distribution of solidification time in different positions of the thin slab, as calculated based on the temperature field. The corner and center regions are enlarged in the figure, and different temperature scales are employed. The closer to the corners, the shorter the required solidification time, as the corners experience two-dimensional heat transfer. At the same time, the portions near the edges have shorter solidification times due to direct contact with the mold. The central region, however, experiences a longer solidification time due to indirect contact with the mold as well as the influence of latent heat release during solidification.
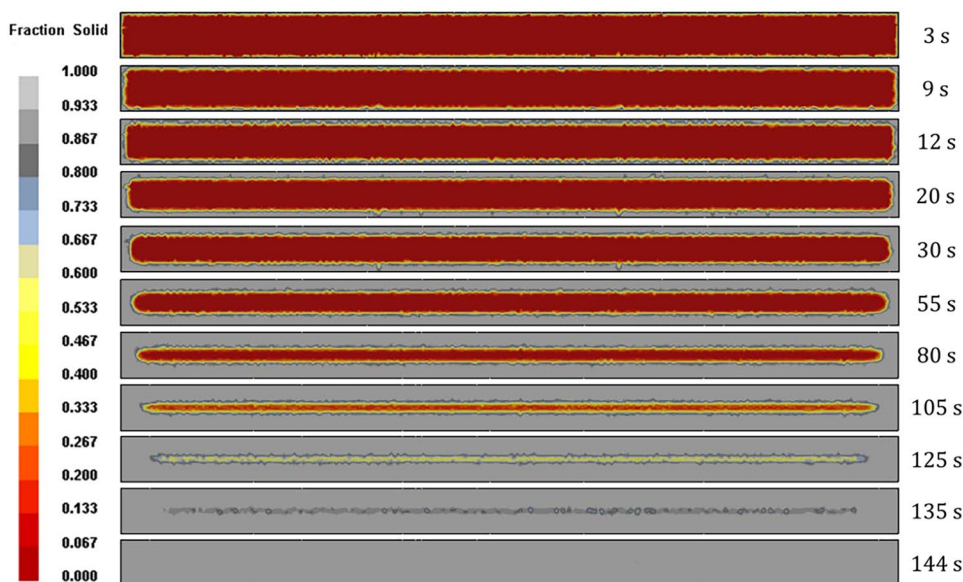
Figure 7 presents a statistical analysis of the solidification time at different distances between the center and the corner/edge. The positions of the corner/edge/center have been marked in Fig. 6. The edge refers to the wide surface of the casting slab and the corner refers to the junction between the wide and narrow surfaces of the slab. The solidification time at the corner is extremely short, approximately 2.1 s (at 0.5 cm away from corner); the solidification time at the edge is also short, approximately 5.6 s (at 0.5 cm away from edge); the central region requires the longest solidification time, approximately 77.5 s. Additionally, due to the two-dimensional heat transfer effect on the corner, the cooling rate is faster, and the curve depicting the change in solidification time with distance grows much slower here than that of the edge. Based on the previous calculation results, the temperature difference across the solid–liquid phase boundary is 61.6 °C. Using the solidification time and the temperature difference across the solid–liquid phase boundary, the cooling rate can be calculated. The cooling rates range from approximately 47–1800 °C/min. The cooling rates at the corners and edges are around 1000 °C/min, while the central part experiences a cooling rate of around 50 °C/min, or even lower.

2.4 In-situ Observation of Solidification and Subsequent Cooling Processes

For further exploration of the solidification and solid-state phase transformation in the thin slab casting process, in-situ observation by HT-CLSM (high temperature confocal laser scanning microscopy) has been conducted based on the aforementioned calculations and simulations. The experiment setup is illustrated in Fig. 8. The samples used in the experiment is cylindrical steel specimens with a
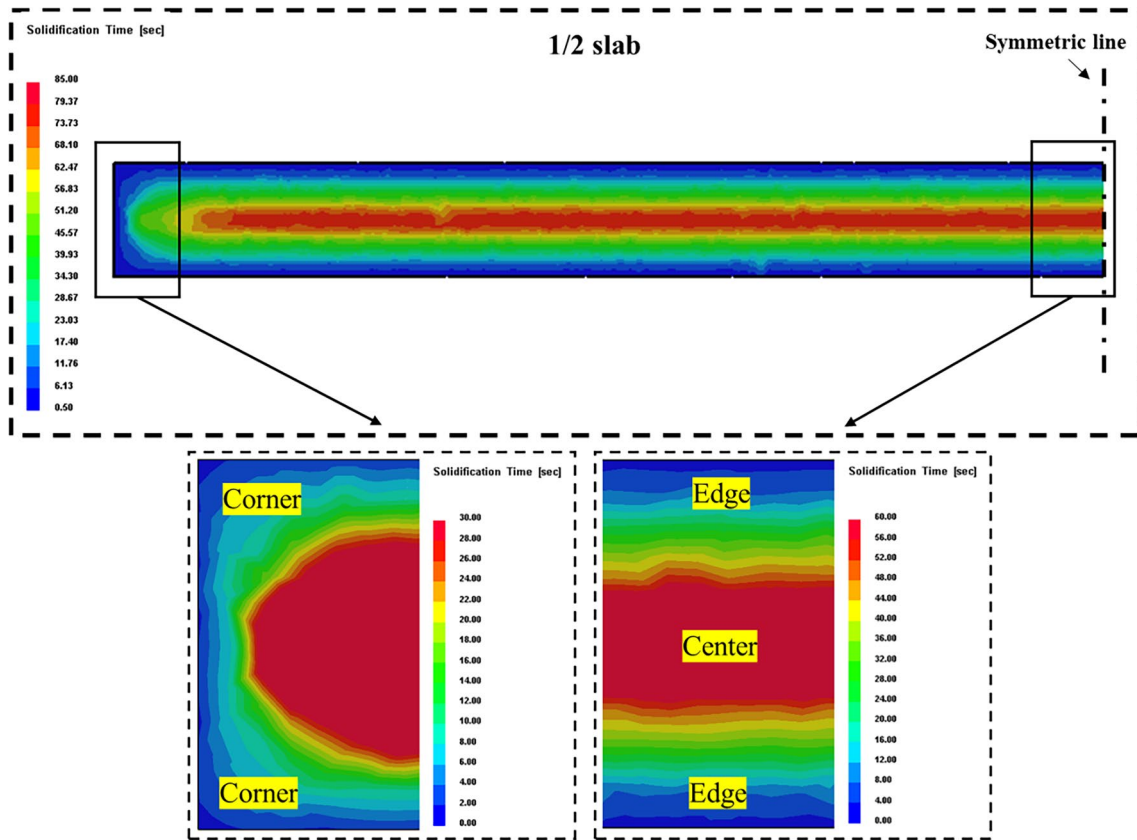
Fig. 5 Numerical simulation results of increasing fraction solid with the passage of casting process (corresponding to an increase in time)

Fig. 6 Simulated solidification time at different positions
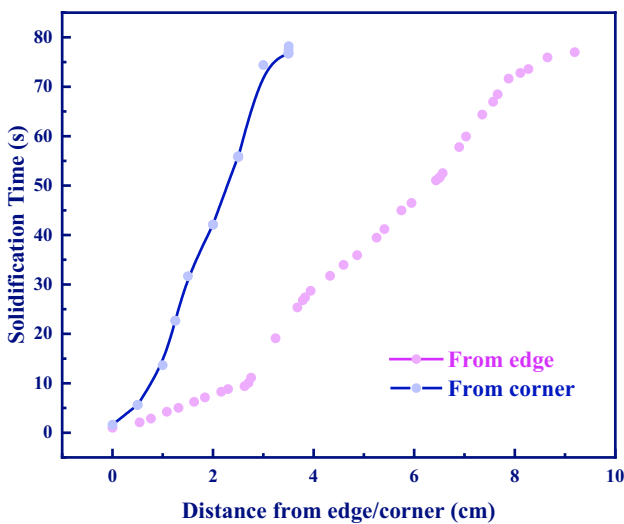

Fig. 7 Solidification time at different distances between the center and the corner/edge

diameter of 5 mm and a height of 2 mm. Their surfaces are polished smooth. During the experiment, the sample is placed in a crucible, and the inner wall of the entire ellipsoidal heating furnace is gold-plated to reflect and
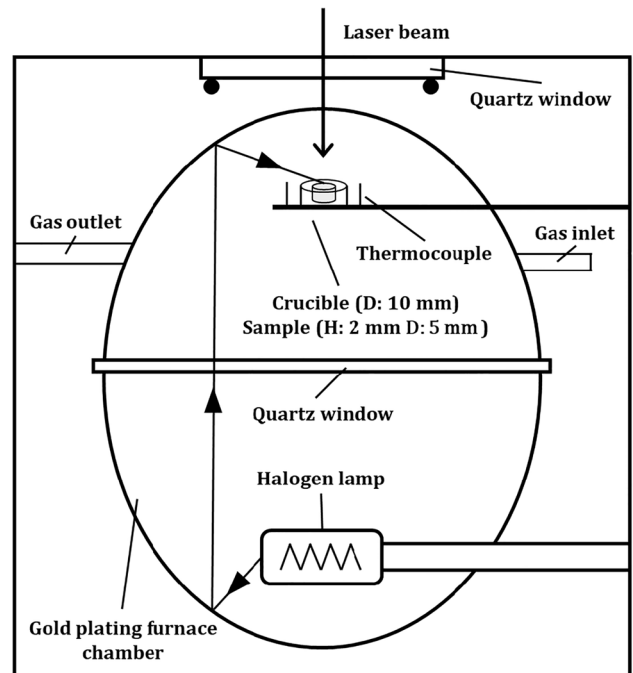

Fig. 8 Principal diagram of in-situ observation of solidification and cooling processes using HT-CLSM

concentrate the heat emitted by the halogen lamp onto the sample. The temperature is measured using a thermocouple, and the entire chamber is filled with argon gas for protection.

Figure 9 illustrates the detailed heating and cooling patterns of high temperature confocal microscopy experiments. Firstly, the sample is heated from room temperature to 1515 °C at a heating rate of 360 °C/min, with intermittent holding during the heating process to prevent rapid increase in crucible temperature. Subsequently, the sample is held at 1515 °C for 3 min to ensure complete melting. Following this, it is cooled to room temperature at preset rates of 1000, 150, 50, or 10 °C/min. The basis for selecting these four cooling rates is the solidification time calculated by numerical simulation, and the cooling rate is calculated based on the required solidification time. The four selected values almost cover the cooling rates of different parts of the thin slab, with higher cooling rates corresponding to the corners of the slab and lower cooling rates corresponding to the center of the slab. The solidification phase transition and solid-state phase transition of the hot stamping steel sample during the cooling process are observed and recorded. The observation is concentrated on the central region of the melt.

After cooling to room temperature, a hemispherical hot stamping steel specimen is obtained in the crucible. The central region of the hemispherical surface is observed under an optical microscope. In cases of severe oxidation or poor depth of field, scanning electron microscopy (SEM) has been employed to observe the sample surface. This process is primarily conducted to observe the dendritic growth under different solidification rates.
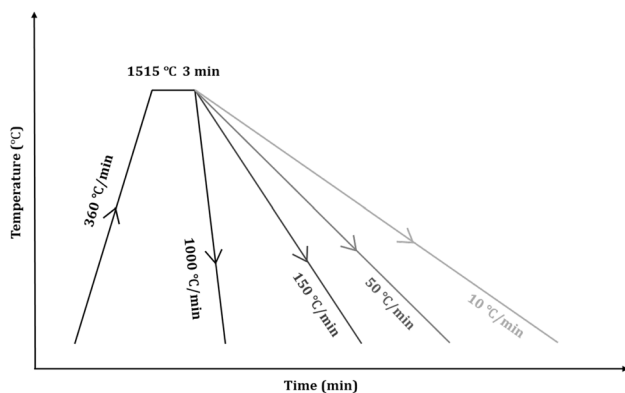

Fig. 9 Temperature control scheme for high temperature confocal microscopy experiments

3 Experiment Results

3.1 High Temperature Phase Transition During Solidification and Cooling Processes at Different Cooling Rates

Taking 50 °C/min and 150 °C/min cooling rates as examples, their solidification and subsequent cooling process are shown in Figs. 10 and 11. These figures represent some typical moments during the entire solidification and cooling process. After the steel sample is heated to complete melting, a hemispherical liquid droplet is formed due to the action of surface tension, and the observed field of view is the upper surface region of the droplet. First is the cooling process at the cooling rate of 50 °C/min, initially, the entire field of view is liquid. When the temperature decreases to 1448 °C, nucleation of the δ-Fe phase begins in the observed area. As the temperature decreases, more and more nucleated δ-Fe phases appear, and at the same time, the phases continue to grow, while the liquid phase gradually decreases. When the temperature drops to 1356 °C, the peritectic reaction occurs, and the remaining liquid phase, along with the already formed δ-Fe phase, transforms into γ-Fe phase. The phase transformation speed is very fast, and numerous cracks are observed on the grains. Subsequently, liquid phase continues to transform into γ-Fe phase until complete transformation. Until the temperature drops to 698 °C, the transformation of γ-Fe to pearlite (α-Fe and cementite) begins, and acicular ferrite is observed growing from the grain boundaries into the interior of the grains. Initially, only a few places undergo phase transformation, but as the temperature continues to decrease, many acicular ferrites grow from the grain boundaries. Meanwhile, diffusion-type phase transformation occurs at grain boundaries and defects, generating cellular ferrites. This phenomenon can be observed in the highlighted area in Fig. 10. At the cooling rate of 150 °C/min, the cooling process experienced by the hot stamping steel is similar to that at 50 °C/min. The main difference is that the temperature of solid-state phase transformation is lower. Moreover, the structures that grow are predominantly acicular ferrites.

3.2 Dendrite Growth During Solidification at Different Cooling Rates

Multiple sets of experiments have been conducted at each cooling rate. Figure 12 depicts different samples obtained from two experiments conducted at a cooling rate of 1000 °C/min. The dendritic growth on the uppermost surface of these samples has been observed.

Even under identical experiment conditions, there are variations in the observation results. In (a), dendrites grow

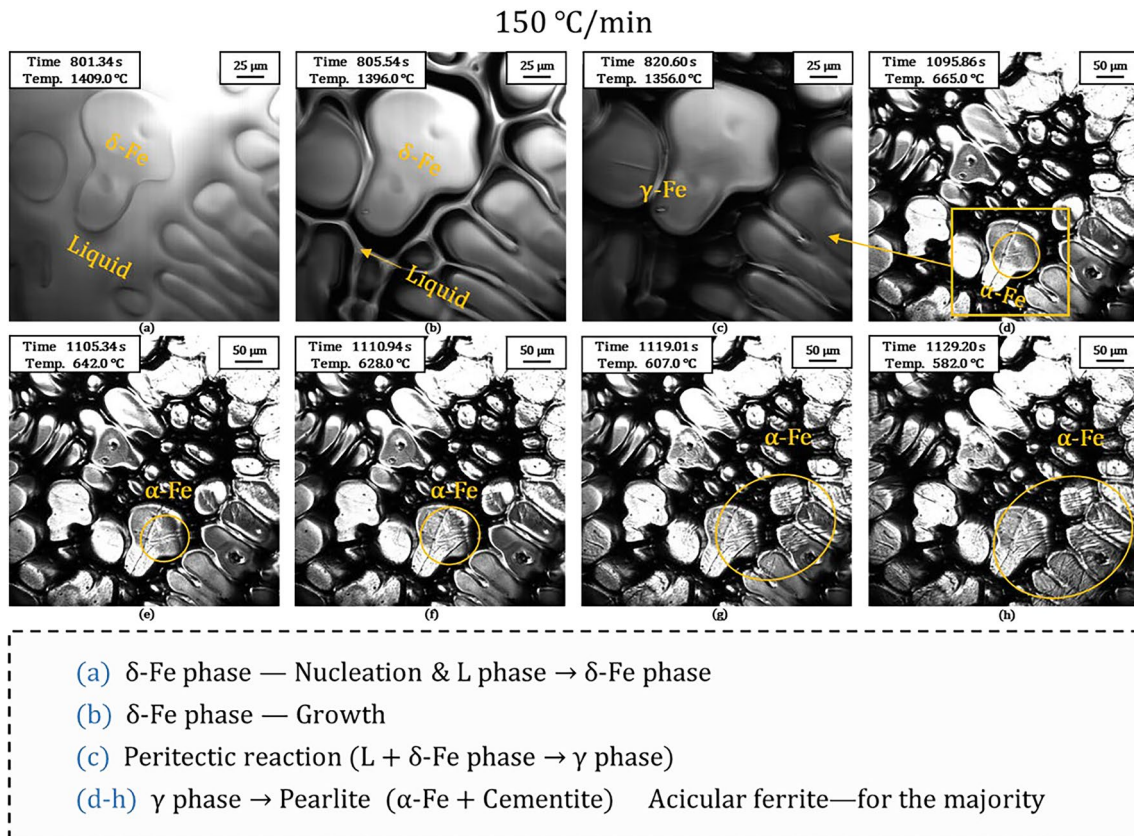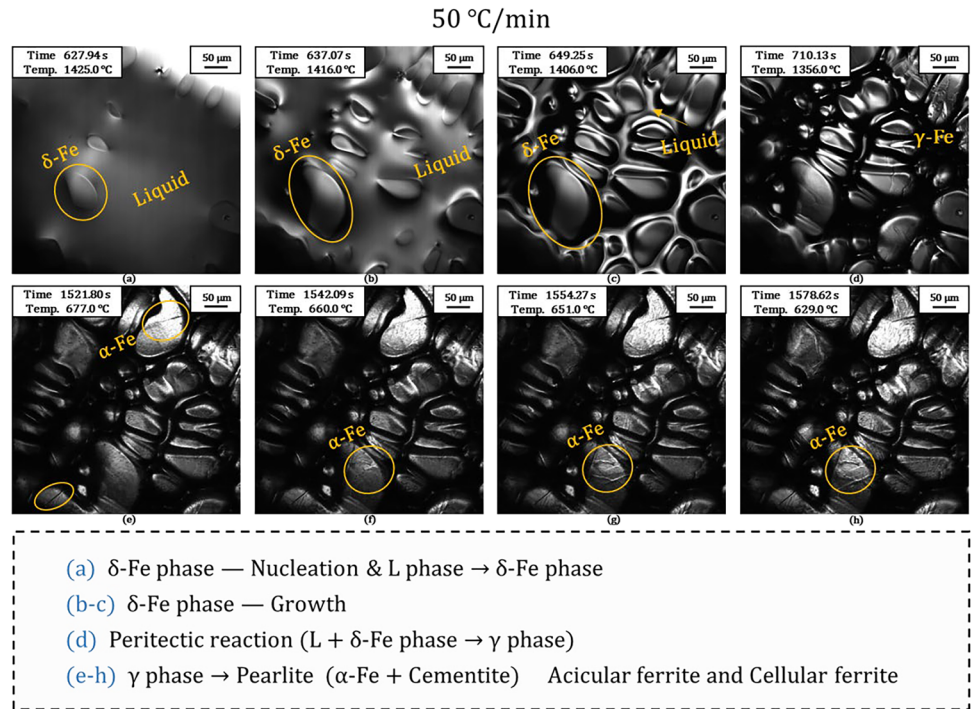**Fig. 10** The complete phase transformation process of hot stamping steel at a cooling rate of 50 °C/min

(a) δ-Fe phase — Nucleation & L phase → δ-Fe phase

(b-c) δ-Fe phase — Growth

(d) Peritectic reaction (L + δ-Fe phase → γ phase)

(e-h) γ phase → Pearlite (α-Fe + Cementite)   Acicular ferrite and Cellular ferrite

(a) δ-Fe phase — Nucleation & L phase → δ-Fe phase

(b) δ-Fe phase — Growth

(c) Peritectic reaction (L + δ-Fe phase → γ phase)

(d-h) γ phase → Pearlite (α-Fe + Cementite)   Acicular ferrite—for the majority

Fig. 11 The complete phase transformation process of hot stamping steel at a cooling rate of 150 °C/min

Fig. 12 Observation of dendritic growth on the top surface of the samples at the cooling rate of 1000 °C/min **a** sample 1 **b** sample 2
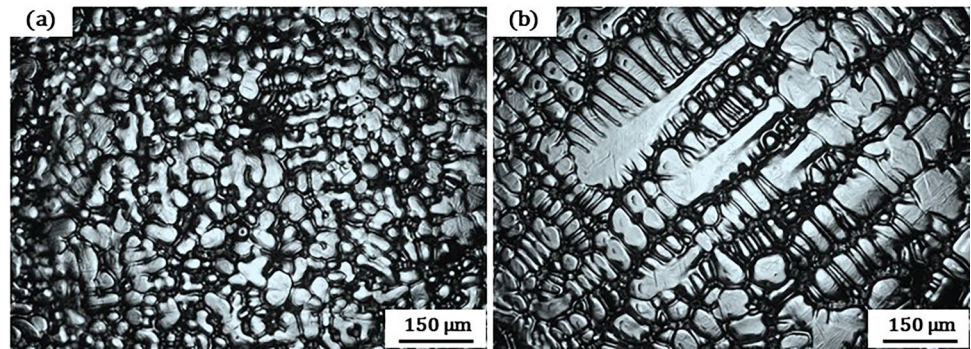
from the surface inward, and only the bottoms of the dendrites, where they aggregate, are observed. In (b), dendrites grow laterally on the upper surface, allowing for a more complete observation of the dendrites. The direction of dendritic growth is opposite to the direction of heat transfer. The different observation results indicate that during the experiment, the direction of heat flux is not only outward from the hemisphere sample but also parallel to the bottom of the sample. The reason may be the changes in the heat transfer direction caused by blowing Ar_2 during the experiment.

In Fig. 13, a shows the optical microscope (OM) result of the sample at a cooling rate of 1000 °C/min, b shows the OM result of the sample at a cooling rate of 150 °C/min, c presents the scanning electron microscope (SEM) result of the sample at a cooling rate of 50 °C/min, and d displays the SEM result of the sample at a cooling rate of 10 °C/min. For samples with higher cooling rates, oxidation is less severe, and the surface is relatively smooth, allowing for effective dendritic observation through OM. However, for samples with relatively slower cooling rates, surface oxidation is more pronounced, and the surface is very rough, requiring observation using SEM after acid etching.
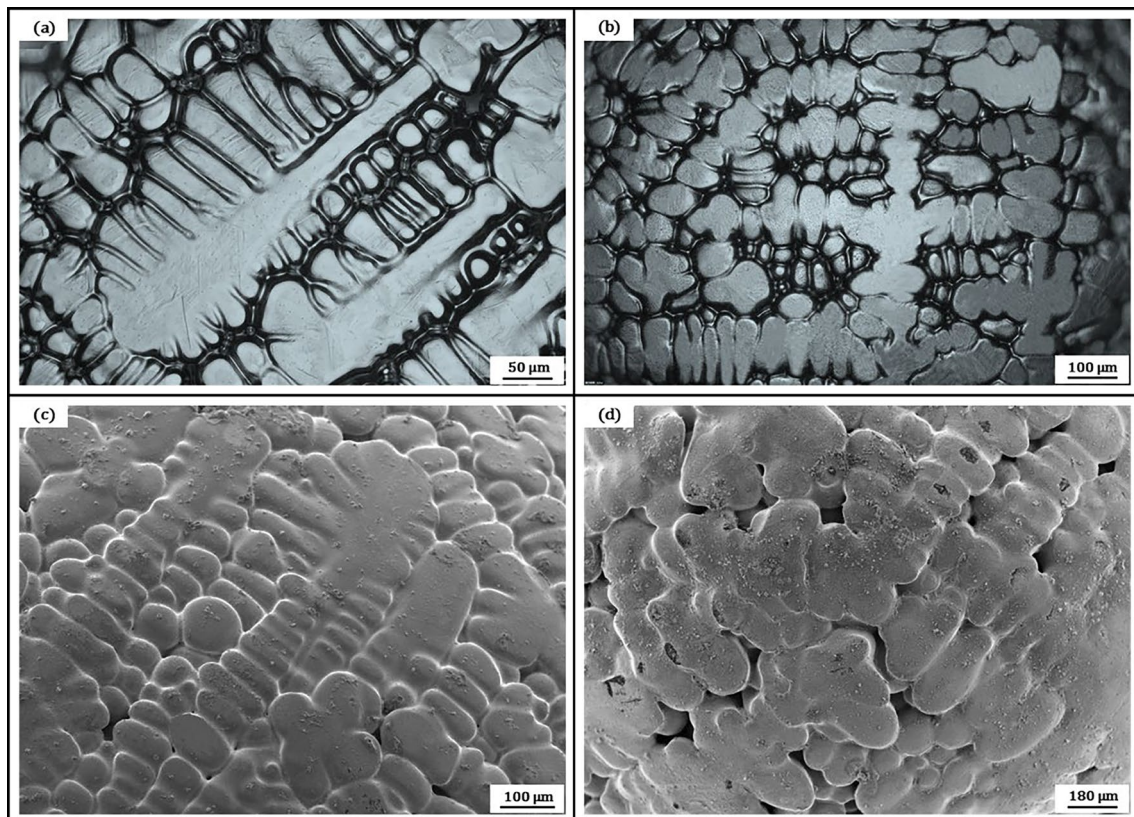

Fig. 13 Observation of dendritic growth in samples **a** 1000 °C/min OM **b** 150 °C/min OM **c** 50 °C/min SEM **d** 10 °C/min SEM

At the cooling rate of 1000 °C/min, dendrite growth appears relatively regular, with secondary dendrites growing from the primary dendrite arms. Due to less compression at the top, dendrites are preserved intact, but on one side, there is less growth due to compression. At the cooling rate of 150 °C/min, dendrites observed at the top closely resemble equiaxed grains, and they are coarser compared to the 1000 °C/min. At the cooling rate of 50 °C/min, dendrites are coarser, and secondary dendrites grow more completely, engulfing and merging with some of the primary dendrite arms, resulting in elliptical-shaped, coarse secondary dendrites visible in the field of view. At the slowest cooling rate of 10 °C/min, secondary dendrites are the coarsest, presenting a more three-dimensional ellipsoidal shape. Primary dendrite arms are no longer observable, only the large secondary dendrites growing in four directions. Additionally, it can be observed that as the cooling rate decreases, the gaps between dendrites continuously increase, reflected in a rougher surface of the sample.

4 Discussion

4.1 High Temperature Phase Transition During Solidification Processes at Different Cooling Rates

The nucleation and growth of γ phase along the L/δ interface is referred to as the peritectic reaction; the process of γ phase growing and thickening towards the liquid phase and δ phase is referred to as the peritectic transformation. The peritectic reaction occurs rapidly at all four cooling rates. The left side of each set of images (Fig. 14) represents before the reaction, while the right side represents after the reaction. Clear cracking phenomena can be observed. At cooling rates of 10, 50, 150, and 1000 °C/min, the reaction times are within 1.01 s, 1.02 s, 0.34 s, and 0.47 s, respectively (subject to limitations in experiment recording precision).

According to the research of Nishimura et al. the solidification process of Fe–0.3C–0.6Mn–0.3Si alloy has been observed in situ using X-ray synchrotron radiation at different cooling rates [19]. The average velocity of the peritectic transformation at the δ/γ interface ranged from several mm/s to 200 mm/s (200 mm/s corresponds to cooling rate of 0.83 °C/s), and a non-carbon diffusive phase transition (block like transformation) occurred at the cooling rate of 0.83 °C/s. According to the study of Nishimura, it can be concluded that the frequency of image recording in this
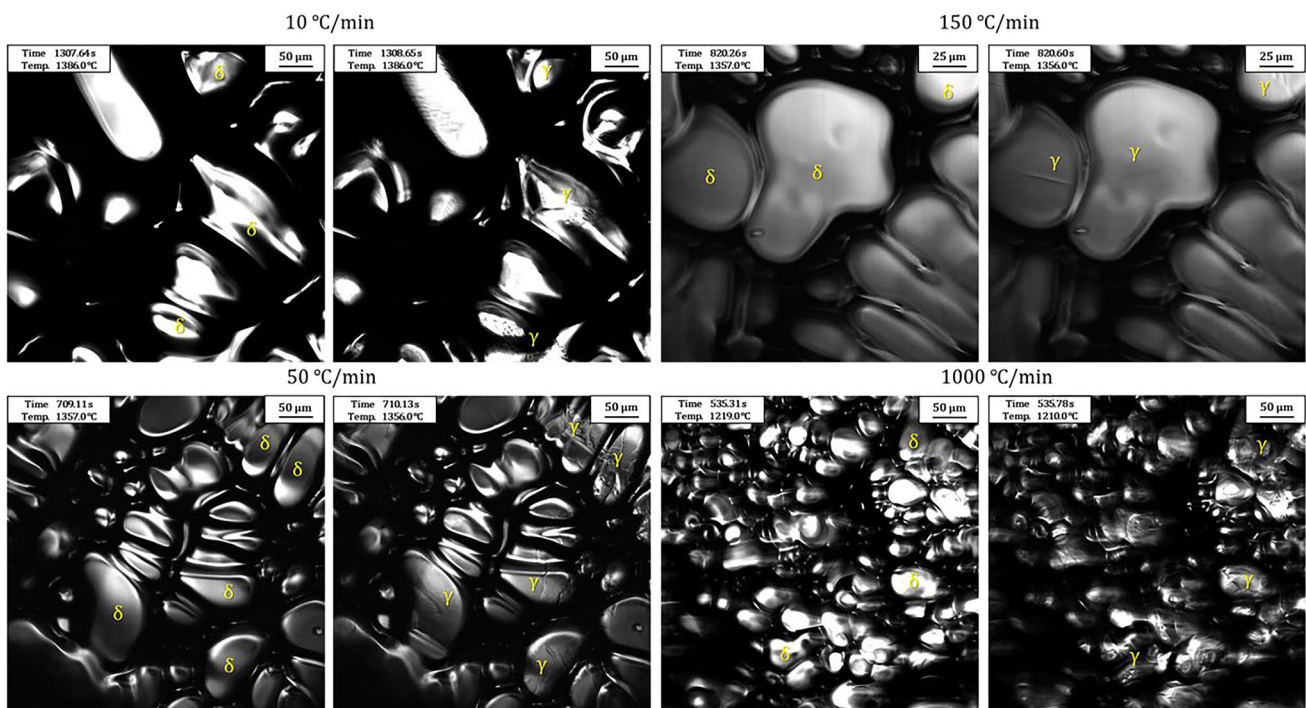

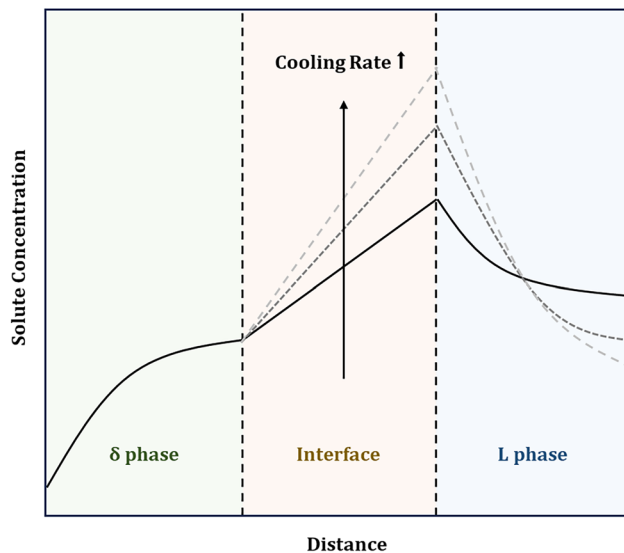**Fig. 14** Peritectic reaction processes at four different cooling rates

Fig. 15 Schematic diagram of concentration distribution at the L/δ phase interface

experiment is too low to capture the process of peritectic reaction, and only the difference between the surface of the sample before and after the reaction can be provided. Therefore, the type of peritectic reaction can only be determined by comparison with literature experiments.

Figure 15 shows the schematic diagram of concentration distribution at the L/δ phase interface.

When the cooling rate is slow, solute atoms form a weak concentration gradient on the L/δ interface. The peritectic γ phase nucleation overcooling is small, and the peritectic phase transformation temperature is close to the equilibrium peritectic phase transformation temperature, resulting in a small thermodynamic driving force for the transformation. This leads to a flat/cellular growth morphology at the transformation interface. Cooling rates of 10 °C/min and 50 °C/min tend to favor this equilibrium diffusion-controlled transformation, this can be proven by Nishimura's research.

At higher cooling rates, the concentration gradient of solute atoms on the L/δ interface becomes steep. The peritectic phase transformation temperature is much lower than the equilibrium peritectic phase transformation temperature, resulting in a larger thermodynamic driving force for the peritectic transformation, leading to blocky transformation. Cooling rates of 150 °C/min and 1000 °C/min exhibit very rapid peritectic reaction rates (blocky transformation), completing the peritectic reaction in 0.4 s or even shorter, not within the set observable range.

The rate of blocky transformation is controlled by the transformation interface process, involving a rapid reorganization of atomic order from one lattice to another. This reorganization occurs much faster than conventional diffusion-controlled transformation. Blocky transformation involves

a significant volume contraction rate, while in non-block transformation, the volume contraction rate is smaller.

Before the nucleation of the peritectic γ phase, δ phase precipitates in L phase, continuously expelling solute, forming a solute boundary layer with a certain concentration at the solid–liquid interface. With increasing cooling rates, the time for solute diffusion from the interface to L phase becomes shorter, resulting in a steeper concentration gradient across the L/δ interface, as shown in Fig. 15.

At the cooling rates of 10 °C/min, 50 °C/min, 150 °C/min, and 1000 °C/min, the temperatures at which peritectic reactions occur are 1386 °C, 1356 °C, 1356 °C, and 1210 °C, respectively. The reaction temperature decreases with increasing cooling rates because the nucleation of the peritectic phase is constrained in the presence of a strong solute diffusion field. The solute gradient at the L/δ interface increases the Gibbs free energy barrier for the nucleation of the peritectic γ phase. The increase in Gibbs free energy leads to an increase in the nucleation overcooling required for the peritectic γ phase. As the cooling rate increases, the concentration gradient across the L/δ interface becomes larger, the nucleation barrier for the peritectic γ phase becomes higher, and the nucleation overcooling required for the nucleation of the peritectic phase increases. Therefore, the reaction temperature for the peritectic reaction decreases with increasing cooling rates.

The differences in peritectic transformation modes and volume contraction rates can lead to uneven growth of the initial solidifying shell during casting especially in the thin slab casting process, making it prone to surface defects [20]. To minimize the occurrence of surface defects in casting, efforts should be made to control the initial solidification cooling uniformly at the curved surface of the mold.

4.2 High Temperature Phase Transition During Subsequent Cooling Processes at Different Cooling Rates

At the cooling rates of 10, 50, 150 and 1000 °C/min, the temperatures at which α-Fe precipitates are 682 °C, 677 °C, 665 °C, and 585 °C, respectively (Fig. 16). Compared to the results from thermodynamic calculation, the temperatures are generally lower. This discrepancy is attributed to the fact that the temperature measurement location during the experiment is slightly below the top of the hemisphere. Therefore, the measured temperatures are slightly lower than those in the actual observation area. The actual phase transition temperatures (PTT) exhibit a good linear relationship with the cooling rate. The relationship between the cooling rate (CR) and the starting temperature of the phase transition can be approximated by the fitted curve (for hot stamping steel: $PTT = -0.0968CR + 681.53$, $R^2 = 0.999$). As the cooling rate increases, the time required for a unit temperature
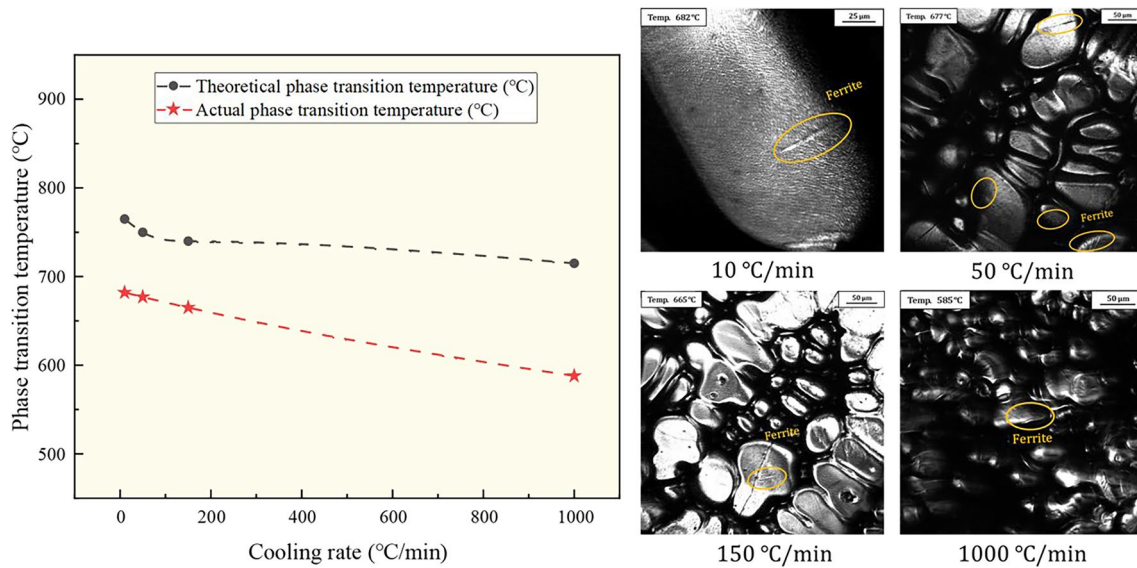
Fig. 16 Pearlite transition temperature at different cooling rates (theoretical and actual experiment values)

reduction decreases and the rate of crystal structure change (from face-centered cubic to body-centered cubic) slows down. The driving force for phase transformation decreases, making α-Fe precipitation more difficult, and more undercooling is required. Consequently, the starting temperature for the transformation from γ-Fe to α-Fe decreases.

Figure 17 illustrates the growth process of acicular ferrite (α-Fe) under the cooling rate of 10 °C/min. Ferrite often nucleates at grain boundaries, as shown by the three laterally grown acicular ferrites and one longitudinally grown ferrite in the figure. This is attributed to the uneven concentration distribution at grain boundaries, which leads to concentration and structural variations. Moreover, grain boundaries are rich in vacancies and dislocations, enhancing the diffusion capability of atoms. Additionally, there is growth of intragranular ferrite: for instance, at 654 °C, a ferrite growing longitudinally gave rise to an intragranular ferrite, and subsequently, some ferrites grew laterally from this base.

Based on the numerical simulation results, it can be concluded that the cooling rate varies in different parts of the slab, resulting in different temperatures in each part when reaching the secondary cooling zone. This leads to different times for ferrite to precipitate at different positions, resulting in insufficient stability of the slab. To address this issue, different secondary cooling water conditions can be arranged at different positions of the casting slab based on numerical simulation results, to achieve uniform temperature distribution of the slab as a whole and eliminate problems caused by local differences.

Simultaneously, the growth rates of acicular ferrite are also recorded under different cooling rates, and a graph of acicular ferrite growth rates with error bars is generated

(Fig. 18). At 1000 °C/min cooling rate, the growth process of complete ferrite is not observed due to excessively rapid cooling. Generally, faster cooling rates result in higher growth rates of acicular ferrite, reaching 8.58 µm/s at 150 °C/min. This phenomenon is attributed to the faster carbon diffusion and increased driving force for ferrite growth at higher cooling rates. Moreover, the analysis of error bars indicates that slower cooling rates lead to smaller statistical errors in growth rates. This implies that slower cooling rates promote more balanced acicular ferrite growth, while higher cooling rates introduce greater growth rate variations.

In the thin slab casting process, the secondary cooling intensity should be adjusted reasonably based on the solidification characteristics of the steel being produced, and the unevenness of the secondary cooling in the cooling zone should be improved. This ensures that the surface temperature of the cast slab avoids the γ–α phase transition temperature range during the straightening section. For hot stamping steel, appropriately increasing the secondary cooling intensity can reduce the precipitation of coarse ferrite along grain boundaries, promote the growth of intra-granular ferrite, reduce the strength difference between grain boundaries and the interior, and thereby enhance the steel's resistance to crack formation.

4.3 Mathematical Relationship Between Secondary Dendrite Arm Spacing and Cooling Rate

With the growth of primary dendrite tip, the size of the secondary dendrite arms gradually increases. At the tip of the primary dendrite, the secondary dendrite arms fill the remaining space along the normal temperature and
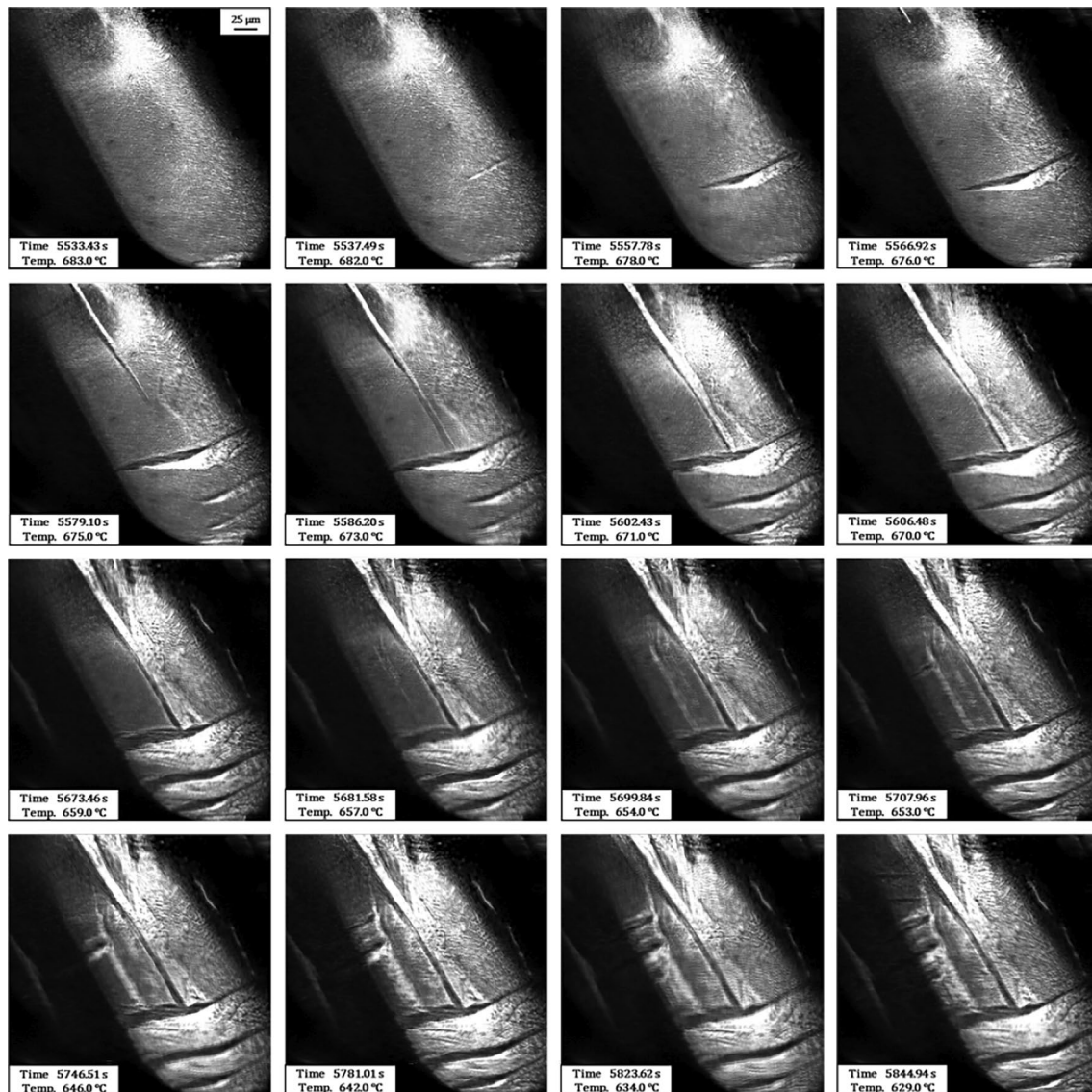
Fig. 17 Growth process of acicular ferrite at a cooling rate of 10 °C/min

composition fluctuations. When the solute fields overlap, the secondary dendrite arms have grown to different sizes. Due to the partial disappearance and growth of some secondary dendrite arms, the spacing between them changes. This entire process continues until the base of the primary dendrite, ultimately resulting in the final spacing between the secondary dendrite arms, denoted as λ_2. Under the cooling rates of 10 °C/min, 50 °C/min, 150 °C/min, and 1000 °C/min, the statistical results for the spacing of secondary dendrite arms are 111.25 μm, 61.52 μm, 51.66 μm, and 27.28 μm, respectively. This indicates that with an increase in cooling rate, the spacing of secondary dendrite arms gradually decreases.

The model proposed by Kattamis and Flemings is used to calculate the spacing between the secondary dendrites [21, 22]:

$$\lambda_2(t_f) = 5.5\left[-\frac{\Gamma_{SL}D_L\ln(C_{eut}/C_0)}{m_L(1-k_0)(C_{eut}-C_0)}\right]^{1/3}\left(\frac{\Delta T_0'}{Gv^*}\right)^{1/3} \quad (1)$$

In this equation:

All variables, except for the cooling rate Gv^*, are constants for a specific alloy composition. Therefore, Eq. 1 can be expressed as a relationship between the spacing of the secondary dendrite arms and the negative one-third
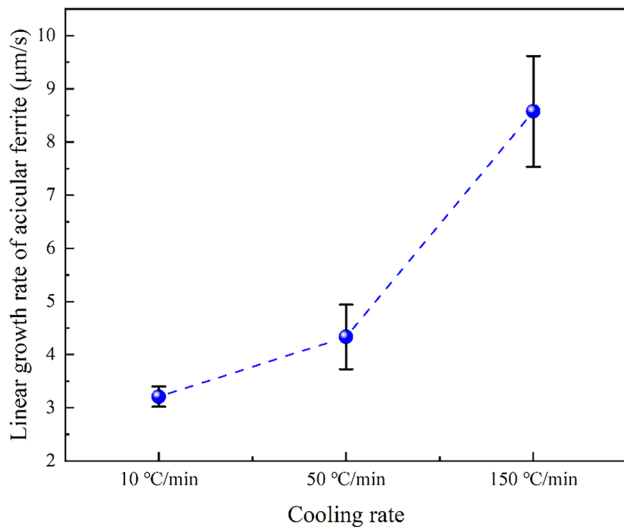
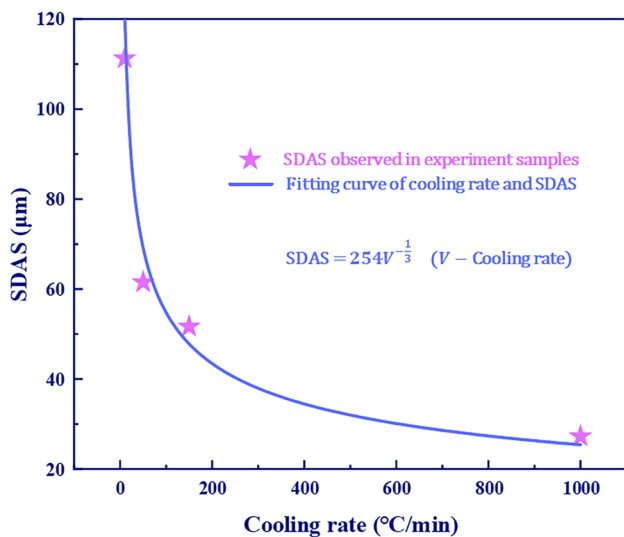Fig. 18 Linear growth rate of acicular ferrite under different cooling rates

Fig. 19 Fitting curve of secondary arm dendrite spacing and cooling rate

power of the cooling rate (as shown in Fig. 19, the unit of cooling rate is °C/min and the unit of λ is μm). Based on this relationship, the spacing between the secondary dendrite arms can be obtained through dendritic corrosion and statistical analysis of the hot stamping steel samples, and subsequently, the cooling rate of the sample at that position can be determined.

5 Conclusions

This article uses ProCAST and HT-CLSM to study the solidification and subsequent cooling process of hot stamping steel at different parts (corresponding to different cooling rates). Based on experiment and simulation results, phase transitions during solidification and cooling processes can be clearly observed, while the functional relationships between the growth rate of hot stamping steel ferrite/secondary dendrite arm spacing and cooling rate are obtained. Additionally, potential optimization strategies for parameters in continuous casting and secondary cooling processes are suggested to enhance the sophistication of thin slab production methods. The main conclusions are summarized as follows:

1. The numerical simulation results indicate that the closer to the corners, the shorter the required solidification time, as the corners experience two-dimensional heat transfer. At the same time, the portions near the edges have shorter solidification times (2.1 s for the fastest) due to direct contact with the mold. The central region, however, experiences a longer solidification time (77.5 s for the lowest) because it does not directly contact the cooling source and is significantly influenced by the release of latent heat during solidification. The calculation of cooling rates at different locations in the casting process of thin slab can be performed based on the numerical simulation results. This analysis can help identify the causes of defects or issues that may arise during the process.

2. In the peritectic phase transformation process, cooling rates of 10 °C/min and 50 °C/min tend to favor this equilibrium diffusion-controlled transformation and cooling rates of 150 °C/min and 1000 °C/min exhibit very rapid peritectic reaction rates (blocky transformation), not within the observable range. The occurrence of blocky transformations during the solidification process primarily takes place in the corners of the casting, so measures need to be taken to address excessive solidification shrinkage in these areas. The differences in the mode of nucleation and the volume shrinkage rate during the recalescence transformation can result in uneven initial solidification shell growth during the casting process of thin slab, leading to surface defects. Efforts should be made to control the uniformity of initial solidification cooling at the curved surface of the mold.

3. The faster the cooling rate, the lower the temperature at which acicular ferrite begins to grow (showing a good linear relationship), and the faster the growth rate of acicular ferrite, reaching 8.58 μm/s at a cooling rate of 150 °C/min. Additionally, slower cooling rates result in

smaller errors in growth rates. Austenitic grain boundary ferrite can deteriorate the thermoplastic properties of steel, regulate the secondary cooling strength reasonably, and weaken the embrittlement effect of grain boundary ferrite.

4. With an increase in cooling rate, the spacing of secondary dendrite arms gradually decreases. The relationship between the secondary dendrite arm spacings and the cooling rate CR are $\lambda_2 = 254CR^{-\frac{1}{3}}$. According to this equation, for hot stamping steel, it is possible to infer the magnitude of cooling rates at different positions of the sample based on the observed dendrite patterns.

References

1. S. Ge, M. Isac, R. Guthrie, ISIJ Int. **52**, 2109–2122 (2012). https://doi.org/10.2355/isijinternational.52.2109
2. A. Taub, E. De Moor, A. Luo, D. Matlock, J. Speer, U. Vaidya, Annu. Rev. Mater. Res. **49**, 327–359 (2019). https://doi.org/10.1146/annurev-matsci-070218-010134
3. X. Jin, Y. Gong, X. Han, H. Du, W. Ding, B. Zhu, Y. Zhang, Y. Feng, M. Ma, B. Liang, Y. Zhao, Y. Li, J. Zheng, Z. Shi, Acta Metall. Sin. **56**, 411–428 (2020). https://doi.org/10.11900/0412.1961.2019.00381
4. S. Niknafs, D. Phelan, R. Dippenaar, J. Microsc. **249**, 53–61 (2013). https://doi.org/10.1111/j.1365-2818.2012.03679.x
5. H. Yasuda, Y. Yamamoto, N. Nakatsuka, M. Yoshiya, T. Nagira, A. Sugiyama, I. Ohnaka, K. Uesugi, K. Umetani, Int. J. Cast Met. Res. **22**, 15–21 (2009). https://doi.org/10.1179/136404609X368118
6. W. Wang, Z. An, S. Luo, M. Zhu, J. Alloys Compd. **909**, 164750 (2022). https://doi.org/10.1016/j.jallcom.2022.164750
7. T. Zargar, F. Sadeghi, J.W. Kim, Met. Mater. Int. **28**, 2263–2276 (2022). https://doi.org/10.1007/s12540-021-01118-z
8. R. Chen, Z. Zheng, N. Li, J. Li, F. Feng, Mater. Charact. **144**, 400–410 (2018). https://doi.org/10.1016/j.matchar.2018.07.034
9. M. Zhu, W. Lou, W. Wang, Acta Metall. Sin. **54**, 131–150 (2018). https://doi.org/10.11900/0412.1961.2017.00430
10. A. Ramírez-López, D. Muñoz-Negrón, M. Palomar-Pardavé, M. Romero-Romo, J. Gonzalez-Trejo, Int. J. Adv. Manuf. Technol. **93**, 1545–1565 (2017). https://doi.org/10.1007/s00170-017-0556-y
11. S. Munusamy, J. Jerald, Met. Mater. Int. **29**, 3423–3441 (2023). https://doi.org/10.1007/s12540-023-01462-2
12. M. Sadat, A. Honarvar Gheysari, S. Sadat, Heat Mass Transf. **47**, 1601–1609 (2011). https://doi.org/10.1007/s00231-011-0822-8
13. I. Dey, R. Saha, S.K. Ghosh, Met. Mater. Int. **28**, 1662–1677 (2022). https://doi.org/10.1007/s12540-021-01058-8
14. S. Nomoto, M. Oba, K. Mori, A. Yamanaka, Integr. Mater. Manuf. Innov. **6**, 69–82 (2017). https://doi.org/10.1007/s40192-017-0083-6
15. Pandat Database Manual. https://computherm.com/docs/PanFe_DB_Manual.pdf
16. ProCAST 2018.0 User's Guide. www.esi-group.com
17. Q. Chen, B. Sundman, Mater. Trans. **43**, 551–559 (2002). https://doi.org/10.2320/matertrans.43.551
18. J. Guo, M. Samonds, J. Phase Equilibria Diffus. **28**, 58–63 (2007). https://doi.org/10.1007/s11669-006-9005-6
19. F. Zhang, C. Zhang, S. Liang, D. Lv, S. Chen, W. Cao, J. Phase Equilib. Diffus. **41**, 793–803 (2020). https://doi.org/10.1007/s11669-020-00834-0
20. K. Dou, Q. Liu, Metall. Mater. Trans. A **51**, 3945–3955 (2020). https://doi.org/10.1007/s11661-020-05819-9
21. K. Dou, Z. Yang, Q. Liu, Y. Huang, H. Dong, High Temp. Mater. Process. **36**, 741–753 (2017). https://doi.org/10.1515/htmp-2016-0022
22. X. Qi, X. Wang, X. Shen, Met. Mater. Int. **29**, 2623–2635 (2023). https://doi.org/10.1007/s12540-023-01402-0
23. T. Nishimura, K. Morishita, T. Nagira, M. Yoshiya, H. Yasuda, IOP Conf. Ser.: Mater. Sci. Eng. **84**, 012062 (2015). https://doi.org/10.1088/1757-899X/84/1/012062
24. S. Abraham, R. Bodnar, J. Lonnqvist, F. Shahbazian, A. Lagerstedt, M. Andersson, Metall. Mater. Trans. A **50A**, 2259–2271 (2019). https://doi.org/10.1007/s11661-019-05148-6
25. T.Z. Kattamis, M.C. Flemings, Trans. Met. Soc. AIME **36**, 1523–1532 (1996)
26. D. Kammer, P. Voorhees, Acta Mater. **54**, 1549–1558 (2006). https://doi.org/10.1016/j.actamat.2005.11.031